PCCP

RSC Publishing

PAPER

View Article Online
View Journal | View Issue

Determination of the phase diagram of water and investigation of the electrical transport properties of ices VI and VII

Cite this: *Phys. Chem. Chem. Phys.*, 2013, **15**, 14364

Bao Liu,*[ab] Jie Yang,[bc] Qinglin Wang,[b] Yonghao Han,[b] Yanzhang Ma[d] and Chunxiao Gao*[b]

Received 10th May 2013,
Accepted 20th June 2013

DOI: 10.1039/c3cp51988k

www.rsc.org/pccp

The phase diagram of water near the ice VI–ice VII–liquid triple point and electrical transport properties of these ices have been studied by *in situ* electrical conductivity measurements in a diamond anvil cell. The obtained phase boundary between ices VI and VII and the melting curve for these ices are in accord with most previous results. The different properties and amount of orientational defects in ice VI and ice VII are associated with abrupt changes in conductivity when a phase transition from ice VI to ice VII occurs. The electrical transport mechanisms of these two ice polymorphs can be understood in terms of the conduction of the already existing ions and Bjerrum defects.

1. Introduction

Water, one of the most abundant substances on Earth, has been intensely studied over hundreds of years. It plays an important role in various geophysical and geochemical processes. For example, its occurrence in minerals not only determines the electrical conductivity of the upper mantle[1] but also influences the formation of minerals.[2] Therefore, studies on the electrical properties and phase diagram of H_2O at high pressure and temperature are crucial for understanding the internal properties of Earth.

Electrical properties of water have been determined by shock-wave experiments,[3–11] which focused on H_2O in a liquid state under ultra-high pressure and high temperature. These shock-wave studies have revealed that a rapid increase in the electrical conductivity of water under pressure was generated by highly mobile charge carriers through chemical ionization[8–10] and then a weak pressure dependence under higher pressure was attributed to complete chemical ionization.[11] In static high pressure experiments, various techniques were used to detect the melting curves of different ices. However, static high pressure experimental results obtained with different melting criteria yielded very different predictions for the melting curves. Bridgman determined melting curves of ices VI and VII up to 3.9 GPa by measuring their volume change with a piston–cylinder device.[12] The appearance and disappearance of the X-ray diffraction peak (110) were used to determine the melting curve of ice VII up to 20 GPa[13] and 38 GPa.[14] The optical observation of melting in ice VII by Datchi *et al.*[15] provided data up to 13 GPa. In a recent study by Lin *et al.*,[16] Raman-active OH-stretching modes and translational modes of H_2O were used to detect melting in ice VII under a pressure of 22 GPa and temperature of 900 K. There are some ice VII melting curves determined by electrical resistance-based measurements. In 1963, Pistorius *et al.*[17] determined the melting curve of ice VII by the resistance drop of an aqueous copper sulfate solution in a simple high-pressure and high-temperature squeezer device. In 1978, Mishima *et al.*[18] determined the melting curve of ice VII by the resistance change of a strain-sensitive manganin wire placed inside the sample in a multianvil pressure device. In these electrical resistance-based studies, the melting curves were determined by the electrical resistivity change of materials other than water itself.

In addition, some static pressure investigations focused on the phase boundary between ices VII and VI.[12,19–21] Earlier phase boundary data were obtained in a piston–cylinder device by measuring the abrupt volume change due to phase transition.[12,21] Johari *et al.*[19] showed that the phase boundary between ices VII and VI is a straight line in the pressure–temperature (*P–T*) phase

[a] *College of Science, Northeast Dianli University, No 169 Changchun Road, Jilin 132012, China. E-mail: liubao@mail.nedu.edu.cn; Fax: +86-432-64806631; Tel: +86-432-64806631*
[b] *State Key Laboratory of Superhard Materials, Institute of Atomic and Molecular Physics, Jilin University, No 2699 Qianjin Street, Changchun 130012, China. E-mail: gaocx599@yahoo.com.cn; Fax: +86-431-85168878-602; Tel: +86-431-85168878-601*
[c] *Fundamental Department, Aviation University of Airforce, Changchun 130022, China*
[d] *Department of Mechanical Engineering, Texas Tech University, Lubbock, Texas 79409, USA*

diagram using an equilibrium pressure method. But by using a differential thermal analysis method, Pistorius *et al.*[20] found the phase boundary to be a curve with the slope changing continuously from 2.4 GPa K^{-1} at 0 °C to 0.57 GPa K^{-1} at 80 °C.

Due to the limitations of the technique, the shock-wave experiments mentioned above have only been used to study the electrical properties of liquid water under very high *P–T* conditions, and there have been no experimental data on the electrical conductivity of water in solid state. In this study, we carried out *in situ* electrical conductivity measurements on ices VI and VII in a diamond anvil cell (DAC). By recording the abrupt changes of electrical conductivity due to phase transitions of water, the phase boundary between ices VI and VII, melting curves of these two phases of ice, and triple point were determined. The electrical transport mechanisms of ices VI and VII were also understood by using the Jaccard theory.

2. Experimental details

High pressure experiments were conducted using a DAC equipped with a van der Pauw type microcircuit. Diamond anvils with a culet of 800 μm in diameter were exploited. Preparation of the microcircuit on the anvil has been reported in our previous works.[22,23] In this study, a 0.3 μm-thick molybdenum film was deposited onto the surface of the upper diamond anvil by a radio frequency magnetron sputtering system and was patterned into a van der Pauw four-probe circuit by a photolithographic method. Then the microcircuit was covered with a 2 μm-thick alumina film and the ends of electrodes were exposed for current loading and voltage recording. To make the electrodes come in contact with the sample, selected areas of the alumina layer were removed and then a detection window was formed on the center of the diamond culet. The sketch of the completed circuit and its photograph are shown in Fig. 1a and b. A sheet of T-301 stainless steel was used as a gasket and was indented to ~100 μm in thickness. For further insulation, an 8 μm-thick mica flake was pressed into the dent. A hole with a 300 μm diameter was drilled into the center of the dent and served as a sample chamber. The sample of deionized water was prepared using a water purification system (KBROI-1010) supplied by KEBANG Water Treatment Engineering Corporation (Hangzhou, China). Deionized water was loaded into the sample chamber of the DAC together with a small (of ~5 μm size) piece of ruby crystal that served as a pressure calibrator. The profile of our designed DAC is shown in Fig. 1c. The resistance of a van der Pauw electrode (both molybdenum thin film electrode and copper wire) is about 100 Ω, which can ensure acceptable accuracy during electrical conductivity measurements. The direct current (DC) was provided by a Keithley 2400 Source Meter, and the voltage drop was measured by a Keithley 2700 Multimeter. During the testing, a constant drive current I_{12} enters the sample through probe 1 and leaves it through probe 2. Then, the voltage drop (V_{43}) was recorded between probe 4 and probe 3. We define the resistance $R_{(12,43)}$ as the voltage drop V_{43} per unit current I_{12}. We define the resistance $R_{(23,14)}$ similarly. Then, the electrical conductivity σ was obtained by the van der Pauw equation[24]

$$\exp(-\pi d R_{(12,43)}\sigma) + \exp(-\pi d R_{(23,14)}\sigma) = 1 \qquad (1)$$

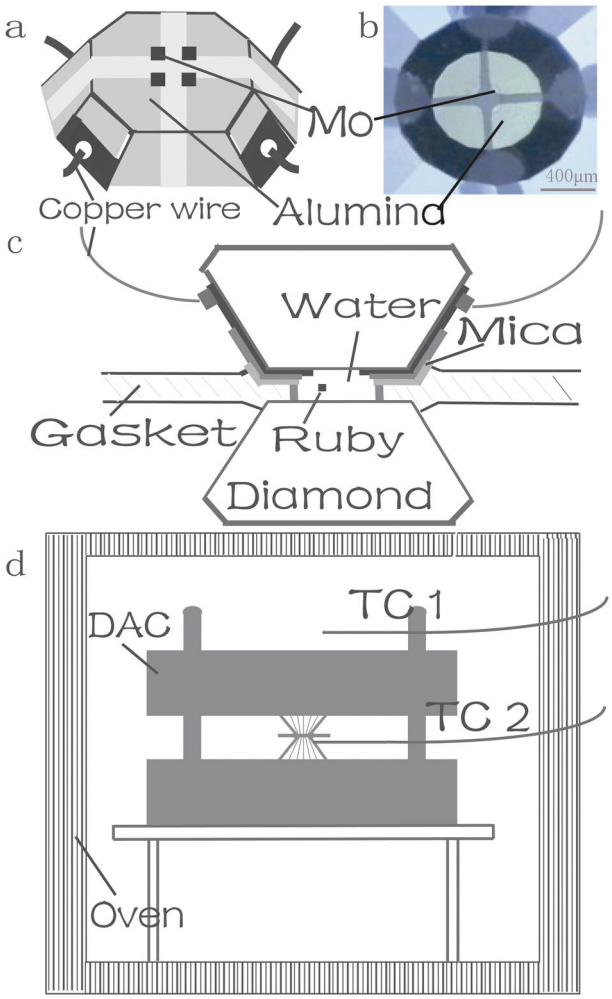

Fig. 1 (a) Van der Pauw microcircuit on a diamond anvil; (b) photograph of the van der Pauw electrodes on a diamond anvil; (c) the profile of the designed DAC; (d) diagram of the designed DAC in the oven. TC 1 and TC 2 are thermocouples 1 and 2, respectively.

Where σ is the conductivity, d is the thickness of the sample, $R_{(12,43)} = V_{(43)}/I_{(12)}$, and $R_{(23,14)} = V_{(14)}/I_{(23)}$. The sample thickness under pressure was determined by a micrometer with the precision of 0.5 μm, and the deformation of the diamond anvils was taken into account.[25]

The temperature control of the DAC was achieved with a PH0307 model forced convection oven, in which temperature was measured by a Chromel–Alumel type thermocouple 1 and was controlled by a feedback power with the uncertainty of 1 K. To take into account the thermal equilibration process after setting the DAC in the oven, another Chromel–Alumel type thermocouple 2 adhered to the diamond anvil was used to ensure the reliability of the temperature measurements. The profile of the designed DAC in the oven is shown in Fig. 1d. Each experimental run of measuring the melting curves of ices VI and VII was conducted by setting the cell at a desired pressure to solidify the water, and after that the temperature was elevated to melt the ice. The temperature was increased by placing the DAC in the oven for about 20 minutes to equalize the temperature between thermocouples 1 and 2 and to

ensure that the sample reached the desired temperature. The melting process of ices VI and VII was monitored by analyzing the curves of the temperature dependence of electrical conductivity. The phase boundary between ices VI and VII was determined by setting the oven at a constant temperature and then increasing the pressure to transform H_2O from VI phase to VII phase. This phase transition was monitored by analyzing the curves of the pressure dependence of electrical conductivity. In the whole experimental process, pressures were estimated using the ruby scale[26] at room temperature with an accuracy better than 0.05 GPa. Ruby R_1 line fluorescence spectra were measured by a Renishaw inVia Raman spectrometer with an argon ion 514.5 nm laser. We calibrate all pressures at room temperature then put the DAC in the oven for electrical conductivity measurements at high temperatures. The use of the ruby fluorescence shift at room temperature to calibrate the pressures at high temperature may introduce errors. The actual pressure of the sample will increase with increasing temperature, which may be caused by the micro-deformation of the anvil and gasket. A temperature correction for the actual in cell pressures (up to 539 K) has been reported by Li *et al.*,[27] who claimed that pressures deduced from the ruby scale for ambient temperature and the yttrium aluminium garnet (YAG) scale for high temperature agree with each other within the uncertainty limits of 0.1 GPa at a maximum pressure of 5.12 GPa. In this study, to be on the safe side, the error limit of pressure determination was increased to 0.15 GPa as a more realistic estimate.

Electrical current is carried by protons in the ice and electrons in the electrodes, which would give rise to space charge layers formed at the ice–electrode interface in DC measurements. In this respect one can say the following. Firstly, ice VI and VII in the DAC are polycrystalline, because there is no ice VI seed crystal in the sample chamber[28] and ice VII is produced through the phase transition of VI → VII at 300 K.[29] The random distribution of the crystal lattice orientation may lead to disordered energy band bending near the interface. Secondly, the grain boundary effect in a polycrystalline sample can also result in the distortion of an energy band near the Fermi level.[30] The macroscopic representation of these two factors is that there is little space charge at ice–electrode interfaces, and if it appears its thickness is very small. To verify whether this test system suffers from a space charge effect at the ice–electrode interface, we tested the contact quality between the electrodes and ice at 3.1 GPa and room temperature (as shown in Fig. 2). The numbers 1, 2, 3, and 4 respectively denote the four van der Pauw type electrodes. Clearly, the linear *I–V* characteristics indicate that the contacts between the electrodes and the ice were almost ohmic. Therefore, we can conclude that, in this DAC system equipped with van der Pauw electrodes, there is no space charge formed at the interface between metal and ice, or the space charge layer is so thin that charge carriers can readily tunnel through it.

3. Results

The triple point was determined by the area surrounded by the three lines (melting line of ice VI, melting line of ice VII, and the phase boundary of ices VI and VII) within the experimental uncertainty. The methods for measuring the melting curves and phase boundary will be described in the two following sections. The area enveloped by the three lines is in the shape of a quasi-triangle, and its center of inscribedcircle is taken as the location of the triple point (as shown in inset of Fig. 3). Thus, the triple point of ice VI–ice VII–liquid is located at 2.2 ± 0.18 GPa and 358.1 ± 4.1 K. These *P–T* values are very close to literature data:[31] 2.216 GPa and 355 K.

A sharp change of the pressure dependence of electrical conductivity will occur due to the phase transition from ice VI to ice VII, then we differentiate the data with respect to pressure and take the peak position and peak width as the transition pressure and error, respectively. For example, Fig. 4a shows the pressure dependence of electrical conductivity of H_2O at 304 K. In the pressure range of 1.94–2.27 GPa, the conductivity increases abruptly. According to the phase diagram of water reported in the literature, the observed sharp increase of electrical conductivity corresponds to the phase transition of H_2O from ice VI to ice VII. Fig. 4b shows the derivative curve of the pressure dependence of electrical conductivity at 304 K. By single peak fitting using ORIGIN software, the peak position of the derivative curve was found to be at 2.105 GPa, which is considered to be the pressure of the phase transition from ice VI to ice VII at 304 K. All the data points on the phase boundary between ices VI and VII are shown in Fig. 3 along with respective experimental error bars.

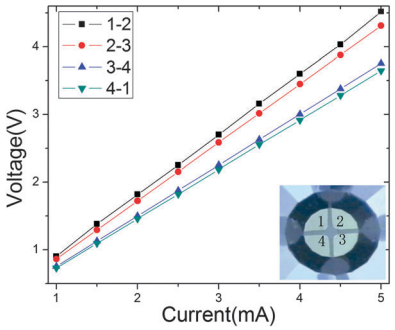

Fig. 2 The *I–V* characteristics of the electrode–ice interface at 3.1 GPa and room temperature.

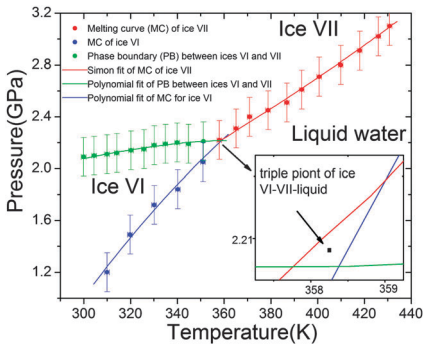

Fig. 3 The phase diagram of water determined by *in situ* high-pressure electrical conductivity measurements. The inset shows an enlarged scale of the phase boundaries near the triple point of ice VI–ice VII–liquid.

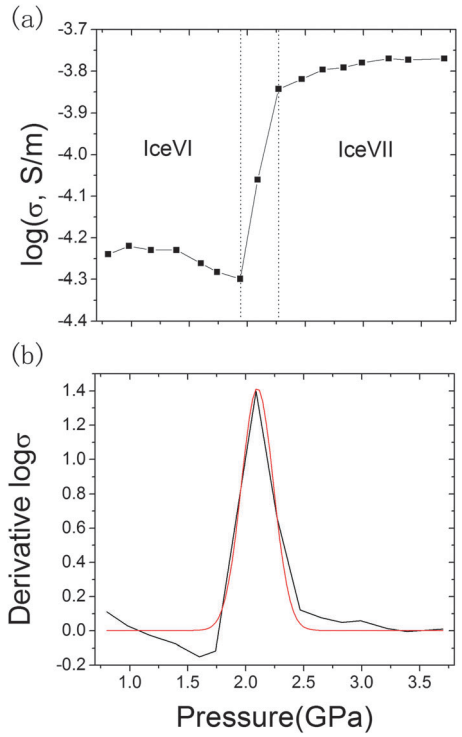

Fig. 4 (a) The abrupt change of the pressure dependence curve of electrical conductivity σ at 304 K when a phase transition from ice VI to ice VII occurs; (b) the pressure derivation curve of electrical conductivity at 304 K (black line) and single peak fitting curve (red line).

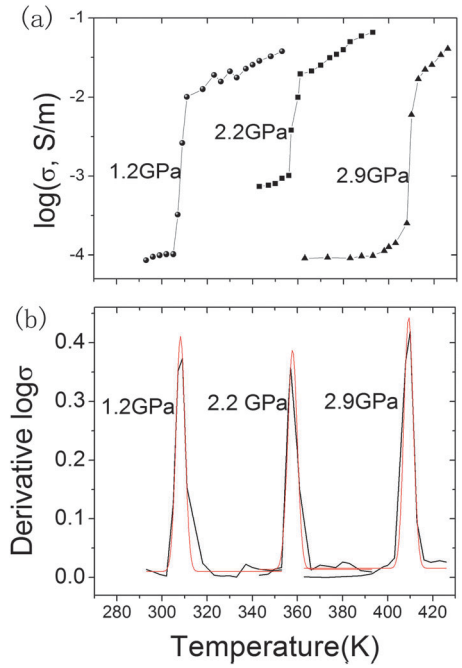

Fig. 5 (a) Representative temperature dependence curves of electrical conductivity σ at 1.2 GPa (circles), 2.2 GPa (squares) and 2.9 GPa (triangles) as the ice melts; (b) the derivative temperature curves of electrical conductivity at selected pressures (black lines) and single peak fitting curves (red lines).

The phase boundary between ices VI and VII is well described by a simple quadratic equation: $P = -1.5631 + 0.02087T - 2.72038 \times 10^{-5}T^2$ with P in GPa and T in K.

One can notice that there is a midway data point at about 2.09 GPa being in neither of the ice VI or ice VII regions in Fig. 4a. By depending only on the electrical conductivity data, we cannot judge whether the midway point is in the ice VI region or ice VII region, or coexisting in both phases ice. The truth is accessible only by *in situ* X-ray diffraction measurements. The midway point between two phases may be associated with the polycrystalline nature of the sample. Phase transitions can bring about the rearrangement of atom positions and result in a lower systematic energy and steadier lattice structure. The DC electrical conduction of the polycrystalline (bulk) sample mainly comes from grain conduction and grain boundary conduction. The phase transition lowers the grain boundary potential barrier, and the grain boundary effect linearly decreases, resulting in the charge carrier transporting more easily through the grain boundary.[32] The grain effect decreasing linearly during the phase transition may result in the midway data point of the electrical conductivity data. Though the grain boundary effect is unavoidable in DC measurements, the agreement between our results and data from the literature implies that the grain boundary effect does not play a very important role in the electrical transportation of ices and DC electrical conductivity measurements on polycrystalline ices can reflect the intrinsic electrical transport properties of ices. Grain interior conduction and grain boundary conduction of a polycrystalline sample can be separated by AC impedance spectroscopy (IS), which would address the problem of the midway data point, which provides motivation for our future work.

The melting curves of ice VI and ice VII were determined by an abrupt increase in electrical conductivity when H_2O experiences a transition from the solid state to the liquid state. Fig. 5a shows the temperature dependence of conductivity of H_2O at 1.2, 2.2, and 2.9 GPa. It can be clearly seen that at each pressure the electrical conductivity increases abruptly by 1–2 orders of magnitude in a narrow temperature range. Fig. 5b shows the derivative temperature curves of electrical conductivity at 1.2, 2.2, and 2.9 GPa respectively. We consider the peak positions as the melting temperatures. All melting points obtained by *in situ* conductivity measurements under high pressure are shown in Fig. 3 along with experimental error bars.

The melting curve of ice VII can be well described by the Simon equation,[33]

$$(P - P_0)/a = (T/T_0)^{\alpha} - 1, \qquad (2)$$

where P_0 and T_0 are respectively the pressure and temperature of the ice VI–ice VII–liquid triple point. The fitted Simon equation according to our data for ice VII is $(P - 2.2)/2.26 = (T/358.1)^{1.78} - 1$. Together with their standard deviations, the parameters a and α have the values 2.26 ± 1.04 and 1.78 ± 0.72, respectively. Ideally, the melting curve drawn according to the Simon equation should be above all liquid points and below all points characterized as solid states. Here, the Simon fit algorithm derives the parameters a and α by minimizing the number of points that lie on the wrong side of the melting curve.

Due to the large deviations in fitting the melting curve of ice VI to the Simon equation, a simple quadratic equation was used in this study instead of the Simon equation. This equation for the melting curve of ice VI has the form $P = -12.24314 + 0.06392T - 6.58313 \times 10^{-3}T^2$ with P in GPa and T in K.

4. Discussion

Fig. 6 shows our results together with those obtained in previous studies. It can be clearly seen that our melting curve of ice VI is in good agreement with the curve measured by Bridgman.[12] For the phase boundary between ices VI and VII, our result is consistent with most previous results within respective experimental error bars, and there is a little discrepancy between the present study and Johari's[19] and Pistorius's[20] works in the lower temperature range. The transition pressures from ice VI to ice VII measured by Bridgman are higher than our results. Bridgman's phase boundary between ices VI and VII was determined by the change in volume of a sample due to the phase transition. When the phase transition from ice VI to ice VII occurs, the volume decreases by 1.03 cm^3 per mole. This change in volume is very slight relative to the ice VII volume of 11.06 cm^3 per mole,[13] which would affect the accuracy of the measurement. Charge carrier transportation is very sensitive to the material's structure, which means that a small change in the structure of the sample could result in a strong response of the sample to the external electric signal.

Our melting lines of ice VI and ice VII are consistent with most previous results[12–16] within respective experimental error bars. They are also in good agreement with the authoritative literature (see eqn (2.19) for the melting curve of ice VI and eqn (2.20) for the melting curve of ice VII in this review article).[31] Thus, our study shows that abrupt changes in electrical conductivity can characterize the melting curves of ices as reliably as previous optical determinations.

We now propose the following reasonable model to understand why the electrical conductivity changes abruptly when the phase transition from ice VII to ice VI occurs. Ice properties related to electrical transport are believed to be dominated by orientational defects. Bjerrum postulated the existence of two kinds of orientational defects, formed by rotation of an OH bond away from its own hydrogen bond axis into that of a neighbor.[34,35] One pair of neighboring O···O atoms is then left with no intervening H atom (an L-defect), while a pair of OH bonds face each other (OH···HO) along the O···O axis of another neighbor (a D-defect). Diffusion of a defect in an ice lattice occurs by rotation of a H–O···H bond. Such defect diffusion in ice plays an important role in the electrical conductivity of ice. It should be noted that ice VI shows the largest H-bond bending of all known phases of ice and the H–O···H angles of ice VII and ice VI have different values.[36] Therefore, the abrupt changes in conductivity (as shown in Fig. 4a), when the phase transition from ice VI to ice VII occurs, should be caused by the different properties and amount of the orientational defects in ice VII and in ice VI.

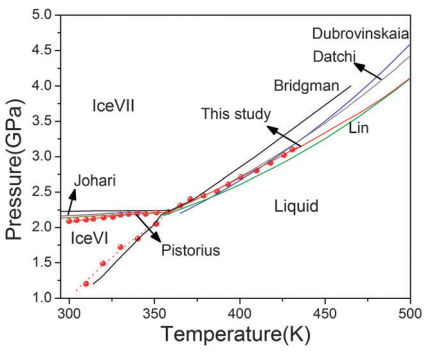

Fig. 6 Phase diagram near the triple point of ice VI–ice VII–liquid shown together with previous results. Red circles: this study; black line: ref. 12; blue line: ref. 14; gray line: ref. 15; green line: ref. 16; violet line: ref. 19; dark yellow line: ref. 20.

We now employ Jaccard's model[37] to gain further insight into the electrical transport mechanisms of ice polymorphs. Jaccard's model proceeds from the assumption that charge carriers in ice are protons, which, to be transferred sizable distances, must go through a succession of jumps, both along hydrogen bonds and from bond to bond. Indeed, any hopping along the bond from one molecule to another will create H_3O^+ and OH^- ions, and any jump from one bond to another will give rise to a pair of Bjerrum defects: L-defects and D-defects. The DC electrical conductivity of ice is determined by all of these kinds of charge carriers, with charges e_i, mobilities μ_i and concentrations n_i (i = 1–4). Let 1, 2, 3, and 4 represent a H_3O^+ ion, OH^- ion, D-defect, and L-defect respectively. Then the respective conductivities are:

$$\sigma_i = |e_i|\mu_i n_i \quad (3)$$

According to Jaccard's theory, the DC electrical conductivity of ice is: $\sigma = \sigma_{ion} + \sigma_B = \sigma_1 + \sigma_2 + \sigma_3 + \sigma_4$. Here σ_{ion} is the conductivity of ions (H_3O^+ and OH^-), and σ_B is the conductivity of Bjerrum defects (D-defect and L-defect). In this study the magnitude of the electric field is in the range of 10^3–10^4 V m^{-1}, which would supply a free proton with energy of about 10^{-5} eV. However, generation of a proton from cracking a hydrogen bond requires energy of approximately 1 eV.[4] Therefore the application of the electric field does not give rise to new protonic charge carriers, but only sets in motion the already existing ions and Bjerrum defects. The carrier concentration n_i is henceforth considered to be a constant quantity in ice. Then according to eqn (3), the electrical conductivities of ices are determined by the carrier mobilities μ_i, which are very low and should be associated with diffusion of orientational defects in ice.[34] As for liquid water, the idea of a significant ionic contribution to electrical conductivity has been widely used in the past. At ambient pressure, the ions in water mainly come from chemical ionization: $2H_2O \rightarrow H_3O^+ + OH^-$. In fact, the lifetime of H_3O^+ ions in liquid water is too short to be observed and even if they occur, their electrical mobility is small compared to that of H^+ ions. Because of this, water at high pressures and temperatures ionizes simply as $H_2O \rightarrow H^+ + OH^-$.[38] The mobility of H^+ and OH^- ions is very high and conduction is induced by the hopping of H^+ and OH^-

ions from molecule to molecule.[39] Besides, application of pressure can enhance chemical ionization in water,[11] which results in an increasing ionic concentration. For these reasons, a significant increase in electrical conductivity by a factor about two orders of magnitude is observed as a result of ice melting (see Fig. 5a). Thus, the differences in electrical transport mechanism lead to a great difference in electrical conductivity of ice and liquid water.

5. Conclusions

Based on *in situ* electrical conductivity measurements using a DAC, the phase diagram near the ice VI–ice VII–liquid triple point and electrical transport properties of ice have been studied. Abrupt changes in electrical conductivity were used to determine the phase boundary between ices VI and VII as well as the melting curve for these ices. Good agreement between our melting lines and those from authoritative literature shows that *in situ* electrical conductivity measurements can characterize the melting curves of ices as reliably as previous optical determinations. The pressure dependence of electrical conductivity of ice indicates that the electrical conduction in ices VI and VII is dominated by already existing ions and Bjerrum defects, which play an important role in the electrical transport properties of ice. The difference in electrical conductivity of ice VI and ice VII is associated with different orientational ordering in these two ice polymorphs. Although there is a possible problem of space charge layers building at the electrode–ice interface in DC measurements, the polycrystalline character of ice would hinder the appearance of a space charge at the ice–metal interfaces.

Acknowledgements

This work was supported by the National Natural Science Foundation of China (Grant No. 11074094, 91014004), by the National Basic Research Program of China (Grant No. 2011CB808204), by the Science and Technology Development Program of Jilin Province (Grant No. 201201106), and by Starting Research Fund for the Doctors of Northeast Dianli University (Grant No. BSJXM-201107).

References

1 S. Karato, *Nature*, 1990, **347**, 272.
2 D. R. Bell and G. R. Rossman, *Science*, 1992, **255**, 1391.
3 M. H. Rice and J. M. Walsh, *J. Chem. Phys.*, 1957, **26**, 824.
4 A. C. Mitchell and W. J. Nellis, *J. Chem. Phys.*, 1982, **76**, 6273.
5 A. Belonoshko and S. K. Saxena, *Geochim. Cosmochim. Acta*, 1991, **55**, 381.
6 K. S. Pitzer and S. M. Sterner, *J. Chem. Phys.*, 1994, **101**, 3111.
7 S. Sakane, W. Liu, D. J. Doren, E. L. Shock and R. H. Wood, *Geochim. Cosmochim. Acta*, 2001, **65**, 4067.
8 H. G. David and S. D. Hamann, *Trans. Faraday Soc.*, 1959, **55**, 72.
9 S. D. Hamann and M. Linton, *Trans. Faraday Soc.*, 1969, **65**, 2186.
10 K. Hollenberg, *J. Phys. D: Appl. Phys.*, 1983, **16**, 385.
11 R. Chau, A. C. Mitchell, R. W. Minich and W. J. Nellis, *J. Chem. Phys.*, 2001, **114**, 1361.
12 P. W. Bridgman, *J. Chem. Phys.*, 1937, **5**, 964.
13 Y. W. Fei, H. K. Mao and R. J. Hemley, *J. Chem. Phys.*, 1993, **99**, 5369.
14 N. Dubrovinskaia and L. Dubrovinsky, *Int. J. High Pressure Res.*, 2003, **23**, 307.
15 F. Datchi, P. Loubeyre and R. LeToullec, *Phys. Rev. B: Condens. Matter*, 2000, **61**, 6535.
16 J. F. Lin, B. Militzer, V. V. Struzhkin, E. Gregoryanz, R. J. Hemley and H. K. Mao, *J. Chem. Phys.*, 2004, **121**, 8423.
17 C. W. F. T. Pistorius, M. C. Pistorius, J. P. Blakey and L. J. Admiraal, *J. Chem. Phys.*, 1963, **38**, 600.
18 O. Mishima and S. Endo, *J. Chem. Phys.*, 1978, **68**, 4417.
19 G. P. Johari, A. Lavergne and E. Whalley, *J. Chem. Phys.*, 1974, **61**, 4292.
20 C. W. F. T. Pistorius, E. Rapoport and J. B. Clark, *J. Chem. Phys.*, 1968, **48**, 5509.
21 A. J. Brown and E. Whalley, *J. Chem. Phys.*, 1966, **45**, 4360.
22 C. Gao, Y. Han, Y. Ma, A. White, H. Liu, J. Luo, M. Li, C. He, A. Hao, X. Huang, Y. Pan and G. Zuo, *Rev. Sci. Instrum.*, 2005, **76**, 083912.
23 M. Li, C. Gao, Y. Ma, Y. Li, X. Li, H. Li, J. Liu, A. Hao, C. He, X. Huang, D. Zhang and C. Yu, *Rev. Sci. Instrum.*, 2006, **77**, 123902.
24 L. J. van der Pauw, *Philips Res. Rep.*, 1958, **13**, 1.
25 M. Li, C. Gao, G. Peng, C. He, A. Hao, X. Huang, D. Zhang, C. Yu, Y. Ma and G. Zou, *Rev. Sci. Instrum.*, 2007, **78**, 075106.
26 H. K. Mao, J. Xu and P. M. Bell, *J. Geophys. Res.*, 1986, **91**, 4673.
27 M. Li, F. Li, W. Gao, C. Ma, L. Huang, Q. Zhou and Q. Cui, *J. Chem. Phys.*, 2010, **133**, 044503.
28 H. Shimizu, T. Nabetani, T. Nishiba and S. Sasaki, *Phys. Rev. B: Condens. Matter*, 1996, **53**, 6107.
29 A. Polian and M. Grimsditch, *Phys. Rev. B*, 1983, **27**, 6409.
30 G. E. Pike and C. H. Seager, *J. Appl. Phys.*, 1979, **50**, 3414.
31 W. Wagner and A. Pruss, *J. Phys. Chem. Ref. Data*, 2002, **31**, 387.
32 Y. Li, Y. Han, Y. Ma, P. Zhu, X. Wang and C. Gao, *Europhys. Lett.*, 2012, **98**, 66006.
33 F. Simon and G. Glatzel, *Z. Anorg. Allg. Chem.*, 1929, **178**, 309.
34 N. Bjerrum, *Science*, 1952, **115**, 385.
35 R. Podeszwa and V. Buch, *Phys. Rev. Lett.*, 1999, **83**, 4570.
36 W. F. Kuhs, J. L. Finney, C. Vettier and D. V. Bliss, *J. Chem. Phys.*, 1984, **81**, 3612.
37 C. Jaccard, *Phys. Kondens. Mater.*, 1964, **3**, 99.
38 W. B. Holzapfel, *J. Chem. Phys.*, 1969, **50**, 4424.
39 M. Eigen and L. De Maeyer, *Proc. R. Soc. London, Ser. A*, 1958, **247**, 505.